



Cite this: *Phys. Chem. Chem. Phys.*, 2023, 25, 142

In situ electrochemical observation of anisotropic lattice contraction of $\text{La}_{0.6}\text{Sr}_{0.4}\text{FeO}_{3-\delta}$ electrodes during pulsed laser deposition†

Christoph Riedl, ‡^a Matthäus Siebenhofer, ‡^{*ab} Sergej Ražnjević, ^c Andreas Ewald Bumberger, ^a Zaoli Zhang, ^c Andreas Limbeck, ^a Alexander Karl Opitz, ^a Markus Kubicek ^a and Jürgen Fleig ^a

$\text{La}_{0.6}\text{Sr}_{0.4}\text{FeO}_{3-\delta}$ (LSF) electrodes were grown on different electrolyte substrates by pulsed laser deposition (PLD) and their oxygen exchange reaction (OER) resistance was tracked in real-time by *in situ* PLD impedance spectroscopy (i-PLD) inside the PLD chamber. This enables measurements on pristine surfaces free from any contaminations and the direct observation of thickness dependent properties. As substrates, yttria-stabilized zirconia single crystals (YSZ) were used for polycrystalline LSF growth and $\text{La}_{0.95}\text{Sr}_{0.05}\text{Ga}_{0.95}\text{Mg}_{0.05}\text{O}_{3-\delta}$ (LSGM) single crystals or YSZ single crystals with a 5 nm buffer-layer of $\text{Gd}_{0.2}\text{Ce}_{0.8}\text{O}_{2-\delta}$ for epitaxial LSF film growth. While polycrystalline LSF electrodes show a constant OER resistance in a broad thickness range, epitaxially grown LSF electrodes exhibit a continuous and strong increase of the OER resistance with film thickness until ≈ 60 nm. In addition, the activation energy of the OER resistance increases by 0.23 eV compared to polycrystalline LSF. High resolution transmission electron microscopy (HRTEM) and X-ray diffraction (XRD) measurements reveal an increasing contraction of the out-of-plane lattice parameter in the epitaxial LSF electrodes over electrode thickness. Defect thermodynamic simulations suggest that the decrease of the LSF unit cell volume is accompanied by a lowering of the oxygen vacancy concentration, explaining both the resistive increase and the increased activation energy.

Received 24th October 2022,
Accepted 27th November 2022

DOI: 10.1039/d2cp04977e

rs.c.li/pccp

Introduction

Lowering the operation temperature of solid oxide fuel and electrolysis cells (SOFCs and SOECs) to intermediate temperatures (450–600 °C) is one of the main goals of current research activities in this field, as operation temperatures enable the usage of cheaper materials, reduce start-up times and improve the long-term stability of the cells.^{1,2} However, virtually all important electrochemical processes in the cells are thermally activated and thus a lower operation temperature inevitably leads to higher resistive losses, limiting the current output and

efficiency of the devices.³ Thus, improved or novel cathode materials are of high importance for a broader application of intermediate temperature solid oxide cells (SOCs).

While currently mostly $\text{La}_{1-x}\text{Sr}_x\text{MnO}_{3-\delta}$ -based or $\text{La}_{1-x}\text{Sr}_x\text{Co}_y\text{Fe}_{1-y}\text{O}_{3-\delta}$ -based cathode materials are applied in SOFCs,⁴ many studies have also investigated numerous other mixed ionic and electronic conducting (MIEC) electrodes, such as $\text{La}_{1-x}\text{Sr}_x\text{CoO}_{3-\delta}$ (LSC),^{5–7} $\text{La}_{1-x}\text{Sr}_x\text{FeO}_{3-\delta}$ (LSF),^{8,9} $\text{SrTi}_x\text{Fe}_{1-x}\text{O}_{3-\delta}$ (STF),^{10–13} $\text{Pr}_x\text{Ce}_{1-x}\text{O}_{2-\delta}$ (PCO),^{14–16} $\text{Nd}_2\text{NiO}_{4+\delta}$ (NNO)^{17–19} or $\text{Sm}_{1-x}\text{Sr}_x\text{CoO}_{3-\delta}$ (SSC)²⁰ in order to test their applicability as SOFC cathodes or SOEC anodes. These materials are promising candidates as electrode materials, but also suffer from disadvantages, such as slow overall oxygen exchange kinetics and/or strong degradation susceptibility. For instance, measurements on dense LSC thin film electrodes revealed very low OER resistances of the surface exchange reaction ($< 1 \Omega \text{ cm}^2$ at 600 °C in air) in their pristine state, but unfortunately also a continuous and severe increase of the OER resistance over time.²¹

A major goal of current research activities on thin film electrodes is an improved mechanistic understanding of the OER on electrode materials and knowledge driven material design of porous, real-life electrodes may greatly benefit from

^a Institute of Chemical Technologies and Analytics, TU Wien, Vienna, Austria.
E-mail: matthaeus.siebenhofer@tuwien.ac.at

^b Centre for Electrochemistry and Surface Technology, CEST, Wr, Neustadt, Austria

^c Erich Schmid Institute for Materials Science, Leoben, Austria

† Electronic supplementary information (ESI) available: Area specific OER resistance plotted vs. electrode thickness of LSF grown on YSZ-GDC (100 nm total thickness). $p\text{O}_2$ dependence of the OER resistance for epitaxial and polycrystalline LSF thin films. Characterization of brownmillerite phase in LSF electrode by HRTEM. GID-XRD of LSF grown on YSZ. See DOI: <https://doi.org/10.1039/d2cp04977e>

‡ Contributed equally.



such fundamental investigations. Recent studies found the surface concentration of different point defects (*e.g.*: electrons, holes, oxygen vacancies) to strongly influence the oxygen exchange rate.^{16,22–24} Thus, tuning defect concentrations of the electrode surface (*e.g.* by surface decorations) will significantly alter the oxygen exchange activity.^{6,23,25} In general, the surface chemistry seems to be a deciding factor for the overall oxygen exchange activity and a wide variety of other modifications such as thermal activation,²⁶ DC polarization²⁷ or liquid surface treatments²⁸ have been used to optimize the surface for the oxygen exchange reaction.

Another approach to alter the oxygen exchange kinetics on oxide surfaces makes use of lattice strain. Impedance measurements on NNO¹⁷ and LSC²⁹ electrodes have shown that tensile strain can accelerate the oxygen exchange activity, while for compressively strained electrodes decreased oxygen exchange kinetics were observed. In several thin film studies under tensile strain, not only faster oxygen exchange kinetics, but also higher concentrations of oxygen vacancies in the bulk of the electrode were found.^{29–31} Similarly, ¹⁸O isotope exchange measurements revealed an enhanced OER rate and a higher oxygen vacancy diffusion coefficient in LSC thin films under tensile strain compared to compressively strained LSC films.^{32,33} In addition, in a recent study, the effect of strain on the surface defect concentrations of LSF was investigated and it was demonstrated that surfaces under tensile strain tend to be considerably more reduced compared to the unstrained state.³⁴ Moreover, HRTEM studies showed oxygen vacancy ordering in LSC films under tensile strain³³ and DFT studies suggested that tensile biaxial strain reduces the oxygen vacancy migration barrier across the system,³⁵ and lowers the oxygen vacancy formation enthalpy.³⁰ The results from these experiments on strained thin films are in good accordance with recent mechanistic studies, which quantified how the oxygen vacancy concentration enters the rate law of the oxygen exchange reaction.^{16,22}

In this study, epitaxial and polycrystalline LSF thin film electrodes were grown stepwise by pulsed laser deposition (PLD) and their OER resistance was measured by *in situ* impedance spectroscopy during pulsed laser deposition (i-PLD). This approach allows one to grow an electrode material and simultaneously perform impedance measurements. Thus, thickness dependent changes of the electrode properties can be tracked during growth, unveiling information which is usually hardly accessible by standard *ex situ* measurements. In addition, i-PLD measurements enable impedance measurements on pristine electrodes free from any external contaminations or electrode degradation, which gives further insights into the electrodes OER kinetics. Employing this technique, an unexpected increase of the OER resistance of epitaxial LSF thin films with increasing film thickness as well as an increased activation energy with regard to polycrystalline films are discovered. Additional high resolution transmission electron microscopy measurements (HRTEM) and X-ray diffraction (XRD) measurements clarify the evolution of the LSF lattice geometry during thin film growth and tie the observed decline of the oxygen exchange kinetics to a continuously decreasing unit cell volume in epitaxial thin films. Considering that a reduced unit cell

volume can lead to an increased oxygen vacancy formation enthalpy, defect thermodynamic calculations are successfully employed to explain the observed increase of the OER resistance and the altered activation energy.

Methodology

Experimental methods

In the course of the experiments, three different substrates were used: (i) (100)-oriented yttria stabilized zirconia (YSZ, 9.5 mol% Y₂O₃, Crystec GmbH, Germany), (ii) (001)-oriented La_{0.95}Sr_{0.05}Ga_{0.95}Mg_{0.05}O_{3–δ} (LSGM) single crystals (both 5 × 5 × 0.5 mm³) grown by the Czochralski technique³⁶ and (iii) YSZ single crystals from (i) with a 5 nm Gd_{0.2}Ce_{0.8}O_{2–δ} (GDC) buffer layer. The GDC buffer layer was deposited *via* pulsed laser deposition (PLD) at a substrate temperature of 600 °C in 0.01 mbar O₂ at a substrate-target distance of 6.0 cm and a laser frequency of 1 Hz. For all i-PLD measurements, Ti/Pt grids (5 nm Ti, 100 nm Pt, 15/5 μm holes/mesh) were prepared on both sides of the substrates by lift-off photolithography and magnetron sputtering. The thin Ti layer acts as an adhesion aid between oxide and Pt. As a counter electrode, nanoporous La_{0.6}Sr_{0.4}CoO_{3–δ} was deposited on one of the Ti/Pt grids (bottom grid) *via* PLD at 450 °C in 0.4 mbar O₂ at a substrate-target distance of 5.0 cm.^{37,38} During the actual i-PLD measurements, La_{0.6}Sr_{0.4}FeO_{3–δ} (LSF) was deposited onto the top Ti/Pt grid *via* PLD at a temperature of 600 °C, a pressure of 0.04 mbar O₂, a substrate-target distance of 6.0 cm and a laser frequency of 2 Hz. For all depositions, a KrF Excimer Laser (λ = 248 nm, Lambda Physics, COMPex Pro 201) with a laser fluence of ~0.9 J cm^{–2} was used.

Impedance spectroscopic measurements inside the PLD chamber were performed on a specially built heating stage³⁹ with an Alpha-A High Performance Frequency Analyzer and Electrochemical Test Station POT/GAL 30V/2A setup (Novocontrol Technologies) in a frequency range from 10⁶ to 10^{–1} Hz. For a more detailed description of i-PLD measurements, the reader is referred to earlier studies employing this technique.^{22,29} The sample temperature was measured *via* the high frequency intercept of the recorded impedance spectra, consisting of the only very slightly temperature dependent wiring resistances of the setup and the Ti/Pt grid as well as the strongly temperature dependent electrolyte resistance.⁴⁰

X-ray diffraction (XRD) measurements were performed with an Empyrean X-ray diffractometer (Malvern Panalytical). For all measurements, a hybrid monochromator was used on the incident beam side and a GaliPIX3D area detector was used in the diffracted beam path (both Malvern Panalytical). Diffractograms were analyzed with Panalytical Highscore.⁴¹ For XRD measurements, samples were deposited with the same parameters without current collecting grids, except for LSF on LSGM, where (due to limited single crystal supply), the i-PLD sample was used during XRD measurements.

Atomic force microscopy (AFM) measurements were performed in tapping mode with a Nanoscope V multimode setup



(Bruker) on a scan range of $1 \times 1 \mu\text{m}^2$, directly after i-PLD measurements on the same samples. The AFM results were evaluated with Gwyddion⁴⁴ to gain information about the surface morphology and crystallinity of the deposited thin films.

The lamella for HRTEM investigations was prepared from the same LSF/LSGM sample which has been measured with i-PLD (*cf.* Fig. 5) by lift-out technique⁴⁵ on a Thermo Fisher Scios 2 DualBeam FIB/SEM with a Ga-ion beam operating at 30 kV accelerating voltage. For final thinning and polishing, the voltage was successively reduced to 5 kV and 2 kV. HRTEM images were acquired using an image-side Cs-corrected JEOL 2100F field-emission transmission electron microscope operating at 200 kV. In order to evaluate lattice parameters, geometrical phase analysis (GPA) technique was used. Each measurement is an average of the area profile spanning about 28 unit cell distances in width ($\approx 11 \text{ nm}$).

Results

Structural characterization and surface morphology

To correlate structural and electrochemical properties of LSF thin films, detailed information on the film structure is required. In this study, polycrystalline and epitaxial LSF thin films are investigated. Polycrystalline LSF thin films have been thoroughly investigated in literature^{46,47} and were grown on YSZ single crystals. In order to realize epitaxial film growth, we used LSGM and YSZ-GDC (YSZ single crystals with a 5 nm PLD grown buffer layer of $\text{Gd}_{0.2}\text{Ce}_{0.8}\text{O}_{2-\delta}$; cube-on-cube alignment) substrates, see sketch in Fig. 1. While for the perovskite based substrate LSGM (orthorhombic, *Imma*), epitaxial growth of LSF is not surprising and was already shown in a previous study,⁴⁸ it is not obvious that LSF can grow epitaxially on GDC. However, studies in literature have already shown the epitaxial growth of the structurally similar LSC on a GDC buffer layer^{42,49,50} with a 45° in-plane rotation. In our study, we could confirm that also LSF can grow epitaxially on YSZ-GDC.

This is demonstrated by X-ray diffraction in θ - 2θ geometry and reciprocal space mapping, as well as atomic force microscopy (AFM). From the θ - 2θ scans in Fig. 2(A) it is apparent, that LSF on both LSGM and YSZ-GDC grows highly oriented along the [001] direction. Moreover, on LSGM, the quasi-cubic *c*-axis lattice parameter is larger (3.947 \AA) than for LSF grown on YSZ-GDC (3.883 \AA). Also, both peaks are broadened, indicating a relatively small crystallite size or a varying lattice parameter. The additional reflexes for LSF grown on LSGM corresponding to LSF (110) and Pt (111) are due to a platinum grid and the LSF film on top, which couldn't be avoided as an i-PLD sample was used for XRD measurements due to limited sample supply. In addition, a reciprocal space map was recorded on LSF thin films grown on LSGM as substrate. The results show that the LSGM single crystal exhibits multiple domains with slightly varying lattice parameters. Furthermore, the LSF film peak is clearly visible below the single crystal reflex, indicating laterally compressive strain of the film. As can be seen in Fig. 2(B), the film peak is not distinctly separated, but is smeared out

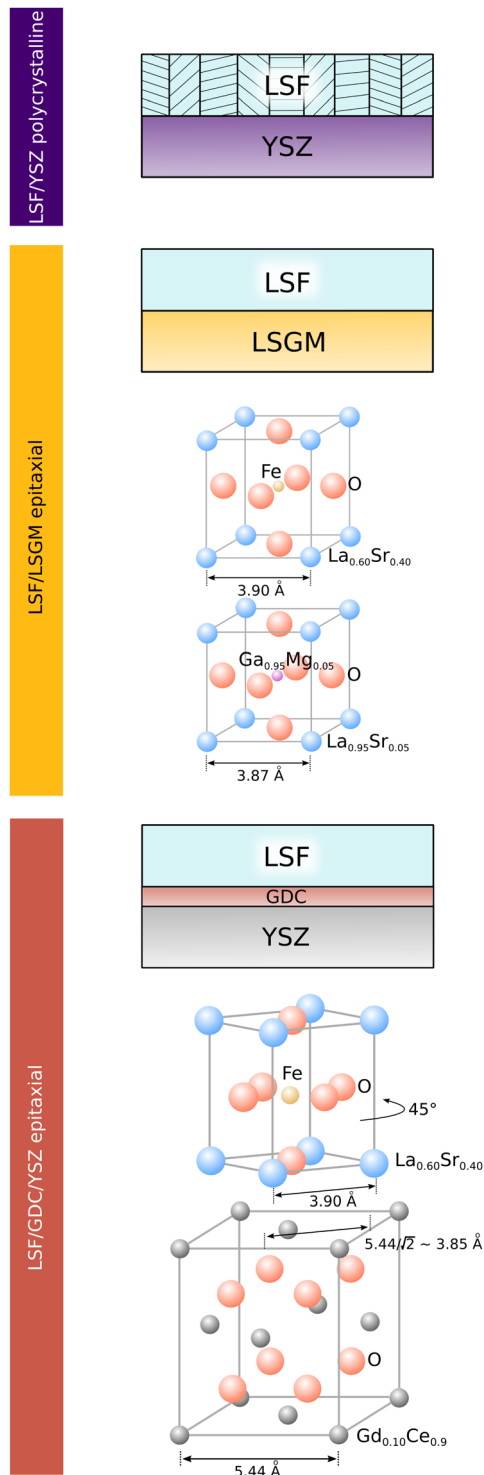


Fig. 1 Sketch showing the structure of LSF electrodes grown on YSZ, LSGM and YSZ-GDC. Lattice parameters of substrates refer to measurements from literature.^{36,42,43}

over a relatively wide range of *c*-axis parameters, which confirms a change of the lattice parameter over the film thickness.

The surface of dense LSF thin films grown on LSGM, YSZ-GDC and YSZ was investigated by AFM, see images in Fig. 4. LSF thin films on both LSGM and YSZ-GDC exhibited very flat



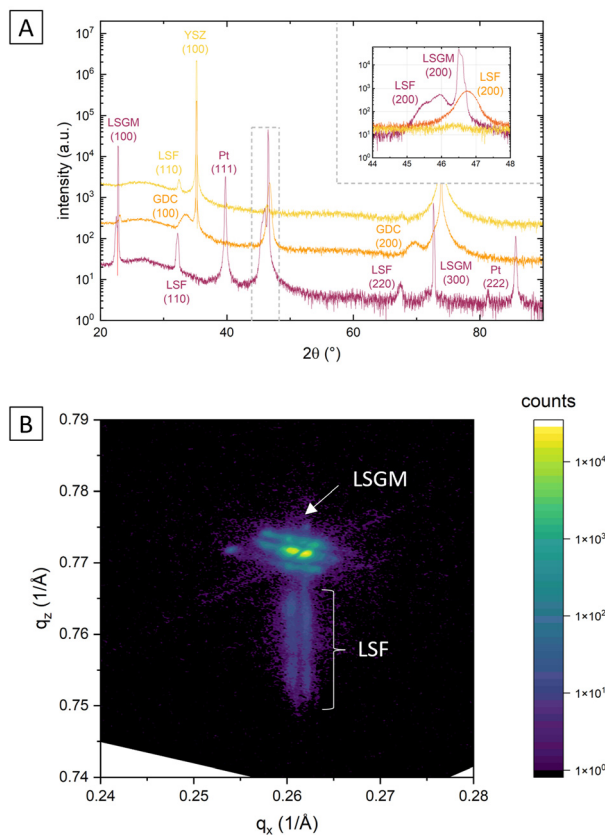


Fig. 2 (A) θ - 2θ scans of LSF on LSGM, YSZ-GDC and YSZ showing oriented growth on LSGM and GDC/YSZ and polycrystalline growth on YSZ; (B) reciprocal space map of an LSF thin film (50 nm) grown on LSGM.

surfaces with a root-mean-square (RMS) roughness of 0.24 nm on LSGM and 0.25 nm RMS roughness on YSZ-GDC. Also, HRTEM measurements (see below) do not show signs of grain boundaries, confirming epitaxial film growth. The surface of LSF grown directly on YSZ, however, showed a strongly granular structure and a comparatively rough surface (5.78 nm RMS roughness). We thus conclude that LSF grows epitaxially on LSGM and YSZ-GDC, oriented in the [001] direction, and in a polycrystalline structure on YSZ single crystals.

i-PLD growth of epitaxial and polycrystalline LSF

In order to understand how the different crystallographic structures of LSF influence the oxygen exchange kinetics, the electrochemical properties of all three types of LSF (on LSGM, YSZ-GDC and YSZ) were tracked by impedance spectroscopic measurements during growth (i-PLD). In Fig. 3, exemplary impedance spectra are shown. All spectra exhibit a real-axis offset at high frequencies corresponding to ohmic resistances of the setup, the Ti/Pt grid and the electrolyte. The spectra in Fig. 3 correspond to a substrate temperature of 600 °C,^{36,51} different off-sets are due to different ionic conductivities of LSGM and YSZ single crystals. Furthermore, one dominant impedance feature was observed in all measurements, which corresponds to the oxygen exchange resistance at the surface of the growing working electrode in parallel to the chemical

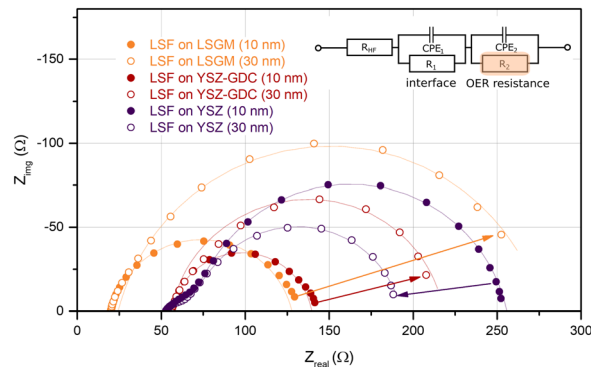


Fig. 3 Impedance spectra (Nyquist plot) of LSF thin films after 2000 and 6000 pulses of LSF deposited on the different substrates LSGM, YSZ-GDC and YSZ, measured at 600 °C in 0.04 mbar O₂. The inset displays the equivalent circuit used for fitting; CPE = constant phase element. $R_1 \parallel CPE_1$ was only required for some of the spectra. The oxygen exchange reaction (OER) resistance R_2 was analyzed in more detail.

capacitance of the thin film.^{13,17,22,52} It is worth mentioning, that samples before LSF deposition also exhibit an impedance curve with one main feature corresponding to the oxygen exchange at the triple phase boundary of the current collecting grid. However, due to the much slower kinetics, the corresponding resistance is in the range of $10^4 \Omega$. Upon growth of the LSF film, significant changes of this low frequency feature were found (see Fig. 5), which will be discussed in detail below. At the high frequency end of the main semicircle a slight shoulder was observed in some measurements, which did not change considerably with film thickness. In literature, similar shoulder-like features were attributed to interfacial resistances between the thin film and the substrate. This interpretation is also supported by the fact that the interfacial resistance was most prominent for LSF grown directly on YSZ, *i.e.* an interface which is prone to reaction.⁵³

Impedance spectra were repeatedly recorded after 1000 laser pulses, corresponding to ~ 5 nm of deposited material. The area specific resistance of the oxygen exchange reaction (OER) was extracted from the main arc (R_2) of the impedance spectra by using the equivalent circuit sketched in Fig. 3. We would like to emphasize that the resistance values found in this study by i-PLD measurements on polycrystalline LSF thin films are about an order of magnitude lower than values usually reported in literature during standard *ex situ* measurements, which is owed to the very clean measurement conditions inside the setup of the i-PLD. This low resistance is a common feature of all i-PLD investigations and was clarified in a recent study.⁵⁴ Trace amounts of sulphur contaminants in the high ppb range are present in most measurement gases and, by fast adsorption on SOFC cathode surfaces, inhibit the oxygen exchange reaction in a variety of ways (site blockage, adsorption behaviour, surface potential change, defect concentration changes).

In Fig. 5, the thickness dependent area-specific oxygen exchange resistance (ASR from R_2) is shown for LSF grown on different substrates. It is apparent that the oxygen exchange resistance develops rather differently for polycrystalline and



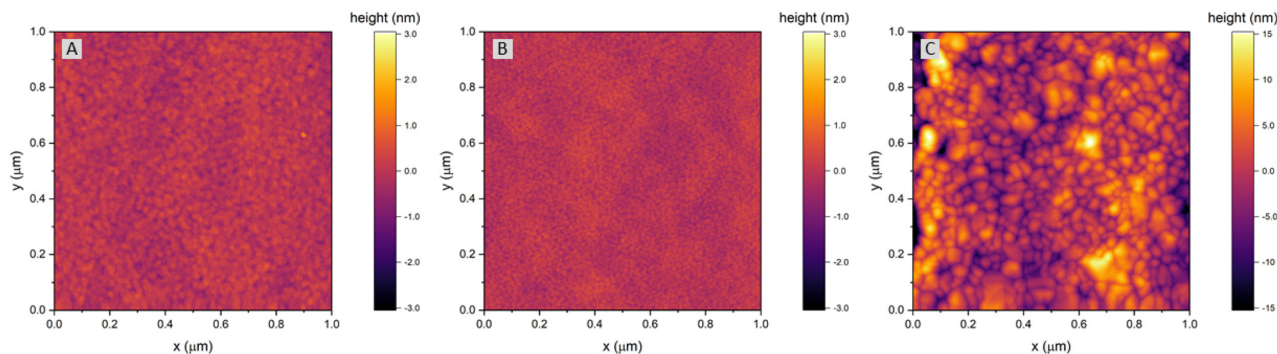


Fig. 4 AFM images of LSF thin films grown on (A) LSGM, (B) YSZ–GDC and (C) YSZ. Please note the different height scale bars for LSF thin films grown on LSGM and YSZ–GDC vs. LSF thin films grown on YSZ.

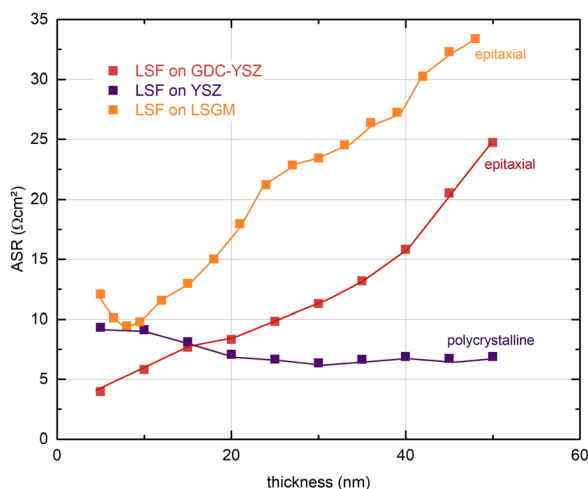


Fig. 5 Thickness dependent area-specific oxygen exchange resistance (ASR) of dense LSF thin films on LSGM, YSZ/GDC and YSZ substrates measured by i-PLD, at 600 °C and 0.04 mbar oxygen partial pressure.

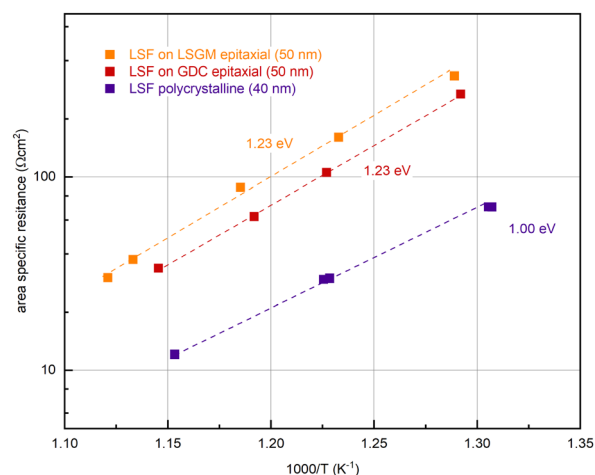


Fig. 6 Determination of the activation energy at an oxygen partial pressure of 0.04 mbar of epitaxial LSF (grown on LSGM (orange) and GDC (red)) and polycrystalline LSF (purple).

epitaxial LSF thin films. On polycrystalline LSF, a slight variation in the beginning is followed by an almost constant OER resistance after around 20 nm. The OER resistances of the two epitaxial thin films grown on LSGM and YSZ–GDC, on the other hand, exhibit a strong increase over film thickness by a factor of about 3–6. This is surprising, as the overall composition of the thin film should not change with its thickness nor should degradation phenomena play a role, since every 5 nm the surface is completely renewed by PLD. This behaviour is also different from epitaxial LSC thin films grown on LSGM, where an earlier study showed a constant ASR after a film thickness of about 30 nm was reached.²⁹

To investigate this process for thicker films, a 100 nm LSF thin film electrode was grown on YSZ–GDC to reveal whether a saturation of the ASR can be observed. Fig. S1 in the ESI† shows that the polarization resistance increases up to a film thickness of about 60 nm and then decreases again, thus excluding bulk transport as the limiting process. This was confirmed by a second experiment, where the high-resistance LSF surface after 50 nm was covered with LSC and the resistance immediately decreased to a value typical for pure LSC. The combination of

these results strongly indicates that the altered kinetics are caused by subtle differences in the LSF surface at different film growth stages.

In further experiments, the oxygen partial pressure and temperature dependence of the OER resistance (R_2) of epitaxial LSF at 600 °C was compared with LSF grown on YSZ. While polycrystalline and epitaxially grown LSF show a very similar pO_2 dependence of the OER resistance (see Fig. S2 in the ESI†), the activation energy differs between the two growth modes (see Fig. 6). On polycrystalline LSF, an activation energy of 1.00 eV was found, on LSF grown epitaxially on LSGM and YSZ–GDC the measured activation energy was considerably increased at 1.23 eV. As shown in ref. 22, the activation energy includes temperature dependences of defect concentrations as well as kinetic barriers. Different activation energies thus do not necessarily indicate a different reaction mechanism (which is also supported by the similar pO_2 dependence). Rather, they can act as a sensitive descriptor of changes in the electrode defect chemistry. The different values found here may thus indicate a shift of the defect thermodynamics. A detailed discussion of the relationship between film thickness, growth



mode, point defect chemistry and ASR will be given in the Discussion section below.

High resolution transmission electron microscopy (HRTEM)

As i-PLD measurements revealed a substantial increase of the OER resistance with film thickness on epitaxial electrodes, HRTEM measurements were conducted to further investigate the structure of the electrode on an atomic level. In Fig. 8, HRTEM images of an LSF thin film grown on LSGM are shown. The interface between LSGM and LSF is clearly visible and HRTEM images confirm that the LSF thin film grows epitaxially and without grain boundaries on the single crystalline LSGM substrate. Moreover, no apparent dislocations were observed in the LSF thin film. It is worth mentioning that local fast Fourier transformation (FFT) found minor amounts of brownmillerite type phase to be present in the thin film, however, it was equally distributed throughout the thin film and no correlation with film thickness was found. Thus, we assume that brownmillerite type phases do not play a decisive role in explaining our measurement results. (FFT patterns can be found in the ESI,† Fig. S3).

In addition, HRTEM measurements also enable the investigation of the LSF lattice parameters at different positions of the thin film. In order to gain statistically meaningful data, the lattice parameters were measured at 15 different lateral positions on the TEM lamella in close proximity to the LSGM interface (5 nm) and 35 nm away from the interface. These measurements reveal that the in-plane and out-of-plane lattice parameter evolve differently with the film thickness (see Fig. 8). The out-of-plane lattice parameter is significantly larger than the in-plane lattice parameter, confirming the laterally compressive strain imposed by the LSGM substrate. For the in-plane lattice parameter, HRTEM measurements found a value of $3.871 \pm 0.006 \text{ \AA}$ close to the LSGM interface, which hardly changed with film thickness ($3.873 \pm 0.008 \text{ \AA}$ at 35 nm). For the out-of-plane lattice parameter, however, a significant change with film thickness was observed. The lattice parameter decreased from $3.973 \pm 0.007 \text{ \AA}$ close to the interface to $3.946 \pm 0.005 \text{ \AA}$ 35 nm away from the substrate, which corresponds to a decrease of the out-of-plane lattice parameter by about -0.68% . Considering that small amounts of strain have shown to alter the oxygen exchange kinetics considerably,^{29,32,55} we believe that this anisotropic lattice deformation could have a strong effect on the surface oxygen exchange kinetics (see below).

In addition, an energy dispersive X-ray (EDX) line profile was acquired to exclude that severe changes of the electrode composition over film thickness influence the electrode OER resistance (see Fig. 7). The interfaces between LSGM|LSF and LSF|Pt protection layer are clearly visible in the EDX line profile images. The platinum protection layer was applied on the electrode surface after electrochemical measurements to prevent damages during the FIB-cut. The interface between LSGM and LSF is not completely sharp which may indicate slight intermixing with the substrate, however, this could also be due to measurement inaccuracies during TEM investigations.

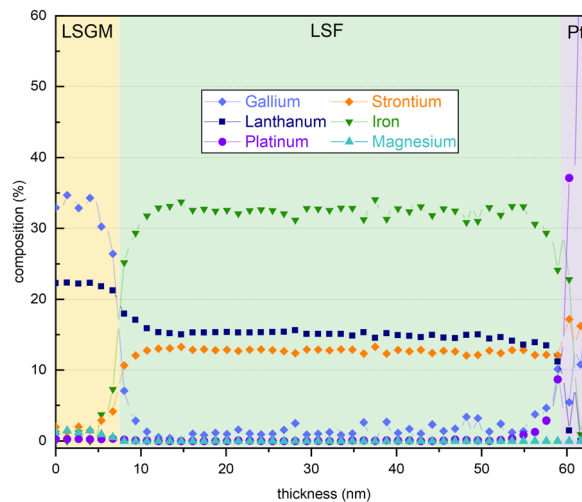


Fig. 7 EDX line scan of an LSF thin film grown on a LSGM substrate with a Pt protection layer.

In conclusion, the EDX analysis reveals that no clear compositional trend is observed in the cation stoichiometry across the film thickness. We also evaluated cation/oxygen ratios but, similarly, they do not show any significant trend with film thickness, rendering a strong change of cation vacancy concentrations unlikely. Thus, we cannot exclude minor changes of cation concentrations in the film but did not find any experimental evidence for significant compositional changes of the electrode which could explain the observed resistance change.

Comparison of lattice parameters and volume on polycrystalline and epitaxial LSF

In Fig. 9(A) the lattice parameters of epitaxial LSF (derived by HRTEM measurements, see Fig. 8) are compared with the pseudocubic lattice parameter of polycrystalline LSF (obtained by $\theta-2\theta$ XRD measurements with the YSZ single crystal lattice parameter used as reference). Based on our HRTEM measurement results, the lattice parameters of epitaxial LSF were approximated assuming a linear relationship to extrapolate the lattice parameter decrease for the entire LSF thin film thickness (*i.e.* 0–50 nm; see dashed orange lines in Fig. 9(A)). For polycrystalline LSF grown on YSZ the lattice parameter is presumed to be constant over the entire electrode thickness (this assumption is supported by grazing incidence XRD measurements of polycrystalline LSF which do not show any peak broadening or other indications of a varying lattice parameter, see Fig. S4 in the ESI†).

From our approximation of the out-of-plane lattice parameter made in Fig. 9(A), the volume of the tetragonal LSF unit cell was calculated (see Fig. 9(B)) and a substantial decrease of the unit cell volume from 0 to 50 nm film thickness by $\approx 1\%$ is found. As the out-of-plane lattice parameter and thus the LSF unit cell volume is the only property for which a significant dependence on the film thickness was measured, we suspect that the variation of this parameter is tied to the increase of the



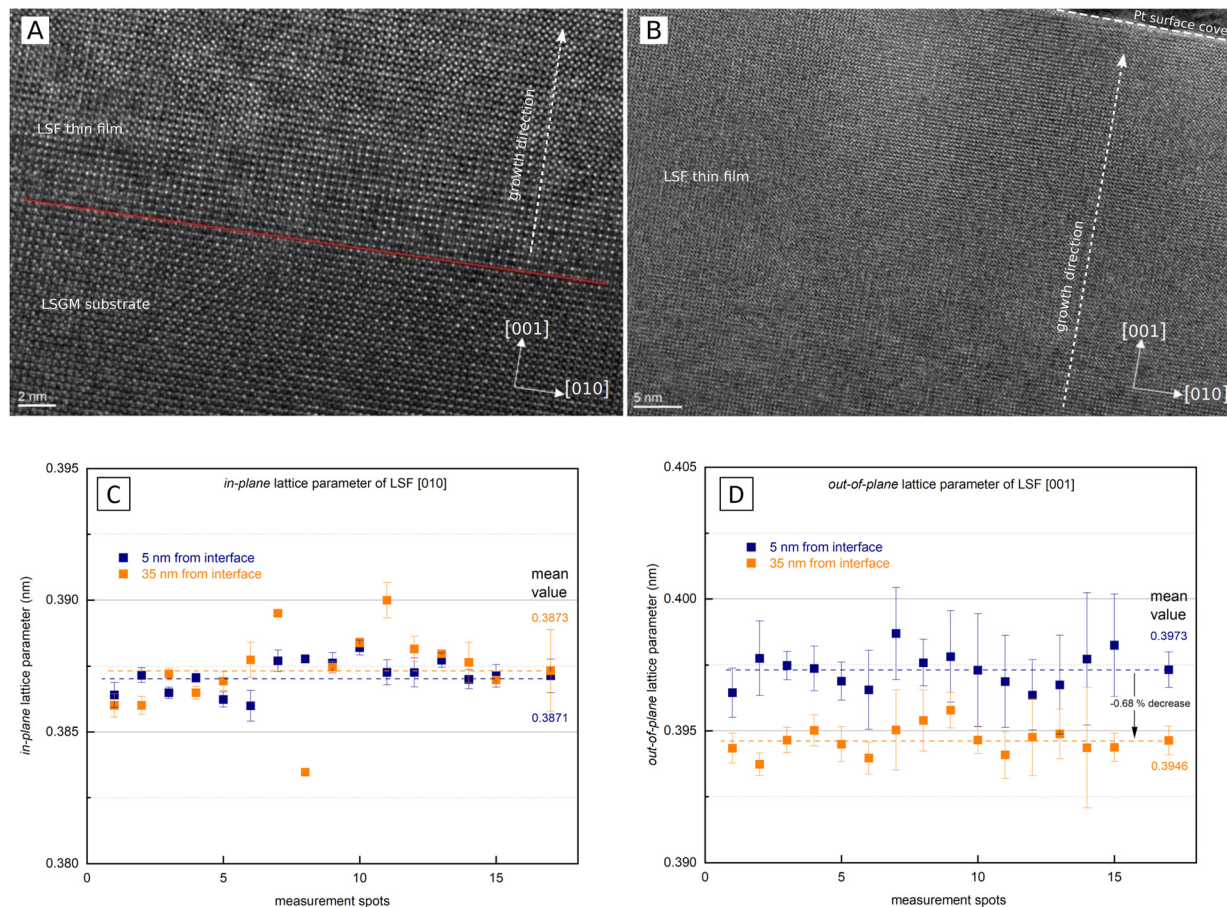


Fig. 8 (A) HRTEM image of the interface region between LSGM and LSF (B) HRTEM image of the LSF thin film (surface near region visible). (C) Lattice parameter in the in-plane [010] direction 5 nm from the LSGM interface (blue) and 35 nm from the LSGM interface (orange). (D) Lattice parameter in the out-of-plane [001] direction 5 nm from the LSGM interface (blue) and 35 nm from the LSGM interface (orange).

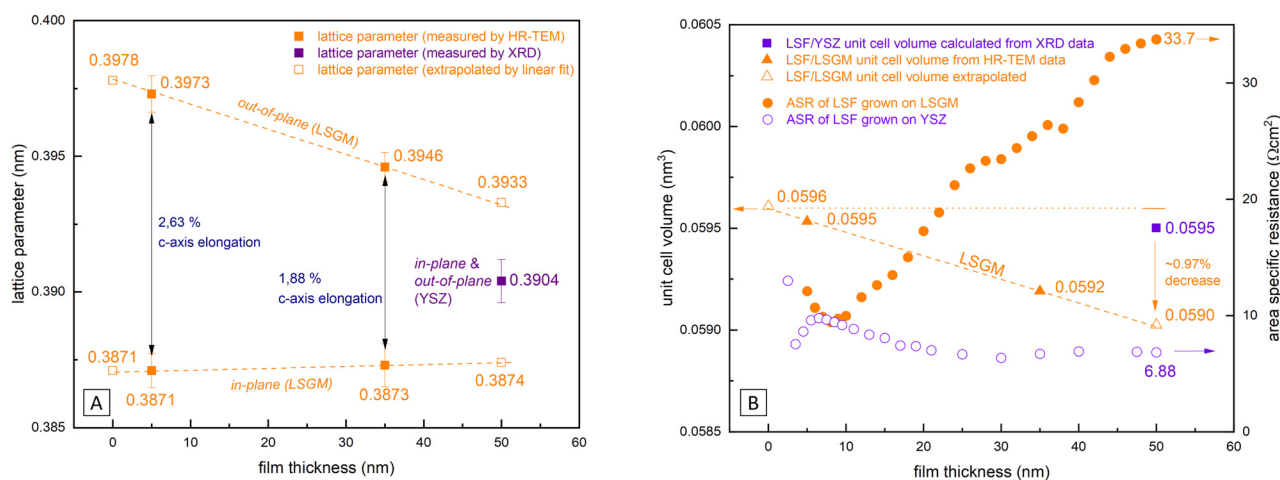


Fig. 9 (A) Comparison of the in-plane and out-of-plane lattice parameters of LSF grown on LSGM measured by HRTEM with the lattice parameter of LSF grown on YSZ measured by XRD are shown. (B) Comparison of the lattice volume of polycrystalline vs. epitaxial grown LSF and the measured ASR.

OER resistance on epitaxial LSF thin films during i-PLD measurements. In the following, we discuss possible effects which may result from this lattice deformation and which might affect the oxygen exchange kinetics.

Discussion

A defect thermodynamic explanation must consider the following experimental results regarding the thickness dependent



electrochemical properties of epitaxial LSF thin film electrodes upon i-PLD growth:

(i) A continuous increase of the OER resistance is observed for epitaxial LSF thin films grown on LSGM or YSZ-GDC substrates, while little variation of the OER resistance is found for polycrystalline LSF electrodes grown on YSZ. At a film thickness of 50 nm the OER resistance of epitaxial LSF (grown on LSGM) is about a factor of 6 higher than that of polycrystalline LSF, (see Fig. 5). Experimental results indicate that this is a surface related phenomenon and not due to bulk transport.

(ii) An increased activation energy (measured at 0.04 mbar O_2) is measured for epitaxial LSF thin films (1.23 eV) compared to a polycrystalline LSF thin film (1.00 eV), (see Fig. 6).

(iii) Similar pO_2 dependencies for polycrystalline and epitaxial LSF indicate that the same mechanism dominates the oxygen exchange reaction on both structures.

(iv) For epitaxial LSF thin films, HRTEM measurements found a decrease of the out-of-plane lattice parameter with increasing LSF film thickness, while the in-plane lattice parameter stayed almost constant. For LSF grown on LSGM, the unit cell volume decreases by about 1% over the entire LSF thin film thickness.

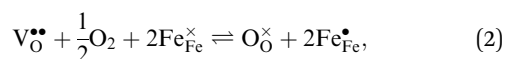
As the oxygen exchange reaction rate on the LSF surface is heavily influenced by point defect concentrations,^{22,56} it stands to reason that the observed changes of the OER resistance are caused by a change of these defect concentrations. Based on literature, we first discuss the defect chemical changes expected from the measured decrease of the LSF unit cell volume over film thickness, *i.e.* how thermodynamic equilibrium constants are affected by lattice strain. Subsequently, we correlate the expected defect chemical changes with the observed OER resistances and activation energies.

Chemical expansion has been intensely studied in literature both on CaF_2 -type and perovskite-type electrodes.^{57–66} Whether the chemical expansion is due to size effects of vacancies or altered cation radii upon oxidation state changes is still under debate. For perovskite-type oxides, numerous studies in literature have found a strong correlation between oxygen nonstoichiometry and the crystal lattice parameters.^{61,63,66–68} A decrease of the unit cell volume is suggested to be accompanied by a decrease of the oxygen vacancy concentration in the material. However, as charge neutrality has to be maintained in LSF electrodes with constant cation stoichiometry, a change of the $V_O^{\bullet\bullet}$ concentration has to be counterbalanced by a change of other point defect concentrations. In general, the concentrations $[i]$ of positively charged point defects (h^\bullet and $V_O^{\bullet\bullet}$) and negatively charged point defects (e' and Sr'_{La}) balance each other in LSF according to

$$[V_O^{\bullet\bullet}] + [h^\bullet] = [e'] + [Sr'_{La}], \quad (1)$$

with e' being negligible in oxidizing conditions.⁵⁶

The equilibrium of the oxygen exchange reaction is given by



$$K_{ox} = \frac{[Fe_{Fe}^{\bullet}]^2 \cdot [O_O^{\times}]}{\sqrt{pO_2} \cdot [V_O^{\bullet\bullet}] \cdot [Fe_{Fe}^{\times}]^2}. \quad (3)$$

Electron holes are often considered as being localized at Fe ions or the surrounding oxygen atoms, indicated by Fe_{Fe}^{\bullet} (Fe^{4+}). Moreover, the Gibbs free energy, enthalpy and entropy of oxygen incorporation (ΔG_{ox} , ΔH_{ox} , ΔS_{ox}) are related to the mass action constant K_{ox} by:

$$K_{ox} = K_{ox}^{\circ} \cdot \exp \frac{-\Delta G_{ox}}{kT} \quad (4)$$

$$\Delta G_{ox} = \Delta H_{ox} - T\Delta S_{ox} \quad (5)$$

The prefactor K_{ox}° includes the concentration of reference states. In a recent study, Lee *et al.*³⁰ demonstrated the dependence of the vacancy formation enthalpy and thus of ΔH_{ox} on the strain state of the electrode. As stated in the equation above, an increase of K_{ox} (= decrease of ΔH_{ox}) triggered by a decrease of the LSF unit cell volume leads to a lowered oxygen vacancy concentration. From eqn (1) and (3), it is further evident that a change of the oxygen vacancy concentration is accompanied by a change of the electron hole concentration.

These alterations unavoidably influence the oxygen exchange kinetics. In literature,^{8,56,69} the following equation was suggested to quantify the different contributions influencing the rates of the OER in forward or backwards reaction:

$$r = r_0 \cdot pO_2^{\nu_p} \cdot \prod_i [i]^{\nu_i} \cdot e^{\frac{\beta e \chi_0}{kT}} \cdot e^{\frac{\beta e \Delta \chi}{kT}} \quad (6)$$

The reaction rate r includes the concentrations $[i]$ of the reacting defect species i (with a mechanism dependent exponent ν_i , describing the number of participating defects), the effect of oxygen partial pressure *via* adsorbates pO_2 (again with a mechanism dependent exponent ν_p , distinguishing atomic or molecular adsorption), the effect of any surface potential χ_0 (which can become relevant if charge is transferred across the surface in this mechanism, represented by a mechanism dependent factor β) or its change upon an applied voltage $\Delta \chi$, and lastly a prefactor r_0 which includes kinetic contributions (chemical activation barriers), but also thermodynamic contributions due to mass action equilibria before the rate limiting step.

In our specific case, we consider the oxygen reduction reaction direction. We assume that the surface potential χ_0 does not vary with pO_2 and lattice volume and that it can be included into r_0 (now r'_0). Since no bias voltage was applied we have $\Delta \chi = 0$. Hence, we obtain $\vec{r} = r'_0 \cdot pO_2^{\nu_p} \cdot \prod [i]^{\nu_i}$. Based on a detailed study on pO_2 and voltage dependent OER resistances, a reaction mechanism was recently proposed for oxygen incorporation into LSF thin films.²² This includes fast molecular oxygen adsorption and first ionization of the adsorbed molecule, followed by a second ionization and dissociation as the rate limiting step. In this case, the rate law for the rate of



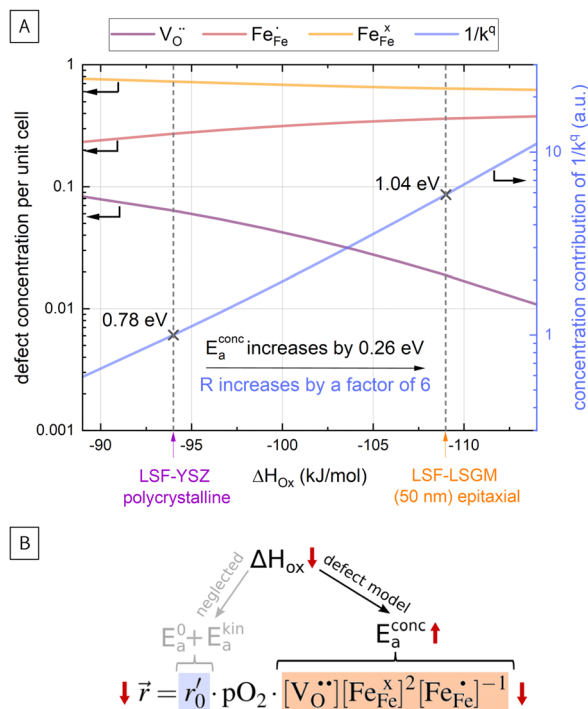


Fig. 10 (A) Calculation of defect concentrations of LSF for different values of ΔH_{ox} ; calculation of the concentration related activation energy ($E_{\text{a}}^{\text{conc}}$) and simulation of the increase of the concentration contribution to the ORR resistance (proportional to the inverse to the surface exchange coefficient), (B) sketch explaining the conducted calculations.

oxygen reduction in eqn (6) can be specified as:

$$\bar{r} = r'_0 \cdot p\text{O}_2 \cdot [\text{V}_{\text{O}}^{\bullet\bullet}] [\text{Fe}_{\text{Fe}}^{\text{x}}]^2 [\text{Fe}_{\text{Fe}}^{\bullet}]^{-1} \quad (7)$$

From eqn (7) it is evident that a decrease of the oxygen vacancy concentration, together with an increase of electron holes, leads to a decrease in \bar{r} , which is equivalent to an increase of the OER resistance.

In Fig. 10(A), the equilibrium concentrations of $\text{V}_{\text{O}}^{\bullet\bullet}$, $\text{Fe}_{\text{Fe}}^{\text{x}}$ and $\text{Fe}_{\text{Fe}}^{\bullet}$ in LSF64 electrodes are simulated for different values of ΔH_{ox} with ΔS_{ox} taken from literature.⁵² According to literature, ΔH_{ox} of a polycrystalline LSF thin film amounts to -94 kJ mol^{-1} .⁵² The predicted concentrations for other ΔH_{ox} values from Fig. 10 can now be used in eqn (7) in order to estimate how much the reaction rate changes when modifying ΔH_{ox} . The sketch in Fig. 10(B) illustrates the changes which we consider or neglect in the simulations. For the sake of simplicity, we neglect any effects of ΔH_{ox} on mass action constants and the kinetic barrier. Then we can determine the change of the inverse reaction rate, *i.e.* the relative change of the OER resistance in dependence of ΔH_{ox} . The corresponding trend of the concentration contribution to the OER resistance is also shown in Fig. 10 (in arbitrary units, indicating changes but not absolute values). In our experiments we find a OER resistance increase in the range of 3–6 (see Fig. 5). According to the plot in Fig. 10(A), a decrease of ΔH_{ox} by 15 kJ mol^{-1} to -109 kJ mol^{-1} decreases the concentration term in eqn (7) ($[\text{V}_{\text{O}}^{\bullet\bullet}] [\text{Fe}_{\text{Fe}}^{\text{x}}]^2 [\text{Fe}_{\text{Fe}}^{\bullet}]^{-1}$)

by a factor of 6 and thus increases the ASR by a factor of six. In other words: a decrease of the oxygen incorporation enthalpy by 15 kJ mol^{-1} can explain the measured resistance change.

Defect concentrations resulting from this change of ΔH_{ox} were also calculated for different temperatures, yielding information on the expected changes of the ASR activation energy. The effective activation energy of the ASR itself is a non-trivial convolution of temperature dependences of all concentrations and of the thermodynamic and kinetic prefactors in the rate equation. A more detailed discussion is beyond the scope of this paper and can be found in literature.²² However, we can estimate how the temperature dependency of the concentration contribution to the OER resistance changes for the adapted ΔH_{ox} value. This analysis shows that the activation energy contribution of the concentrations in eqn (7) increases from 0.78 eV to 1.04 eV , *i.e.* by 0.26 eV when decreasing ΔH_{ox} by 15 kJ mol^{-1} , being very close to our measured change of 0.23 eV and further supporting our assumption that reaction rates change primarily *via* defect concentration changes. Defect simulations of an altered oxidation enthalpy are thus able to explain the results of our i-PLD measurement and also agree with the observations from HRTEM measurements, where a decrease of the LSF unit cell volume was found over film thickness.

The last issue that needs to be discussed is the driving force of the observed lattice contraction which is yet unknown. We can only speculate that a small amount of dislocations might play a role in this structural change which has not been found by HRTEM and which affect the out-of-plane lattice parameter. Also, slight cation stoichiometry changes, which have gone unnoticed in EDX measurements, might contribute to the observed changes of the out-of-plane lattice parameter. Still, as a lattice volume change usually goes hand in hand with an altered oxygen vacancy concentration, it is difficult to discuss the causality of these phenomena and the initial driving force remains unclear.

Summarizing the discussion, we presented a defect chemical model to explain the effect of lattice strain on the electrode defect concentrations and the resulting changes of the oxygen exchange kinetics and its activation energy. i-PLD measurements allowed us to precisely elucidate the effect of lattice strain on the oxygen exchange kinetics and showed that complicated structural changes can occur during epitaxial thin film growth, which have a substantial effect on the electrochemical properties of the thin film surface. It clearly shows that controlling the strain state is a valuable way for tuning the electrochemical material properties, but also emphasizes that the growth of epitaxial thin films requires a great amount of care to ensure the desired properties in the final thin film.

Conclusion

The OER resistances of epitaxial LSF thin films on LSGM or YSZ-GDC and of polycrystalline LSF thin film electrodes on YSZ were measured during growth by *in situ* PLD impedance



measurements. Results reveal that for epitaxial thin films, the OER resistance strongly increases with film thickness, up to a factor of six between 5 nm and 50 nm. The OER resistance of polycrystalline LSF electrodes, on the other hand, is hardly film thickness dependent. In addition, the activation energy of the OER resistance is significantly increased in epitaxial films. HRTEM and XRD measurements reveal a decrease of the out-of-plane lattice parameter with film thickness in the epitaxial films, which leads to a volume contraction of about 1% in 50 nm. Defect thermodynamic calculations suggest that the volume contraction of the unit cell leads to a decrease of the oxygen vacancy concentration with increasing film thickness, which subsequently causes an increased OER resistance. These defect chemical changes also are reflected in an increase of the activation energy which is in excellent agreement with experimental results. This study thus illustrates the potentially severe effect of lattice strain on the electrochemical properties of thin films, emphasizing the importance of strain for the development of highly optimized electrode and electrolyte materials in solid oxide cells and draws attention to the complexity of epitaxial thin film growth and the fact that epitaxy alone does not warrant reproducible electrochemical properties.

Conflicts of interest

There are no conflicts of interest to declare.

Acknowledgements

The authors thank the Austrian Science Fund (FWF) project number: P31165 – N37 and P31654 – N37 for financial support. We also thank Huber Scientific for providing measurement equipment. We gratefully acknowledge support from the K1-COMET center CEST (Centre for Electrochemical Surface Technology, Wiener Neustadt) funded by the Austrian Research Promotion Agency (FFG, award number 865864).

References

- J. A. Kilner and M. Burriel, Materials for Intermediate-Temperature Solid-Oxide Fuel Cells, *Annu. Rev. Mater. Res.*, 2014, **44**, 365–393.
- A. Tarancon, Strategies for Lowering Solid Oxide Fuel Cells Operating Temperature, *Energies*, 2009, **2**, 1130–1150.
- E. D. Wachsman and K. T. Lee, Lowering the Temperature of Solid Oxide Fuel Cells, *Science*, 2011, **334**, 935–939.
- S. P. Jiang, Development of lanthanum strontium cobalt ferrite perovskite electrodes of solid oxide fuel cells – A review, *Int. J. Hydrogen Energy*, 2019, **44**, 7448–7493.
- G. M. Rupp, A. Schmid, A. Nenning and J. Fleig, The Superior Properties of $\text{La}_{0.6}\text{Ba}_{0.4}\text{CoO}_{3-\delta}$ Thin Film Electrodes for Oxygen Exchange in Comparison to $\text{La}_{0.6}\text{Sr}_{0.4}\text{CoO}_{3-\delta}$, *J. Electrochem. Soc.*, 2016, **163**, F564–F573.
- N. Tsvetkov, Q. Lu, L. Sun, E. J. Crumlin and B. Yildiz, Improved chemical and electrochemical stability of perovskite oxides with less reducible cations at the surface, *Nat. Mater.*, 2016, **15**, 1010–1016.
- J. Y. Koo, H. Kwon, M. Ahn, M. Choi, J. W. Son, J. W. Han and W. Lee, Suppression of Cation Segregation in $(\text{La,Sr})\text{CoO}_{3-\delta}$ by Elastic Energy Minimization, *ACS Appl. Mater. Interfaces*, 2018, 8057–8065.
- A. Schmid, G. M. Rupp and J. Fleig, How To Get Mechanistic Information from Partial Pressure-Dependent Current–Voltage Measurements of Oxygen Exchange on Mixed Conducting Electrodes, *Chem. Mater.*, 2018, **30**, 4242–4252.
- M. Kuhn, S. Hashimoto, K. Sato, K. Yashiro and J. Mizusaki, Oxygen nonstoichiometry, thermo-chemical stability and lattice expansion of $\text{La}_{0.6}\text{Sr}_{0.4}\text{FeO}_{3-\delta}$, *Solid State Ionics*, 2011, **195**, 7–15.
- A. Nenning and J. Fleig, Electrochemical XPS investigation of metal exsolution on SOFC electrodes: Controlling the electrode oxygen partial pressure in ultra-highvacuum, *Surf. Sci.*, 2019, **680**, 43–51.
- S. L. Zhang, D. Cox, H. Yang, B. K. Park, C. X. Li, C. J. Li and S. A. Barnett, High stability $\text{SrTi}_{1-x}\text{Fe}_x\text{O}_{3-\delta}$ electrodes for oxygen reduction and oxygen evolution reactions, *J. Mater. Chem. A*, 2019, **7**, 21447–21458.
- V. Metlenko, W. Jung, S. R. Bishop, H. L. Tuller and R. A. D. Souza, Oxygen diffusion and surface exchange in the mixed conducting oxides $\text{SrTi}_{1-y}\text{Fe}_y\text{O}_{3-\delta}$, *Phys. Chem. Chem. Phys.*, 2016, **18**, 29495–29505.
- W. Jung and H. L. Tuller, A New Model Describing Solid Oxide Fuel Cell Cathode Kinetics: Model Thin Film $\text{SrTi}_{1-x}\text{Fe}_x\text{O}_{3-\delta}$ Mixed Conducting Oxides—a Case Study, *Adv. Energy Mater.*, 2011, **1**, 1184–1191.
- D. Chen, S. R. Bishop and H. L. Tuller, Praseodymiumcerium oxide thin film cathodes: Study of oxygen reduction reaction kinetics, *J. Electroceram.*, 2012, **28**, 62–69.
- H. Tuller, S. Bishop, D. Chen, Y. Kuru, J. J. Kim and T. Stefanik, Praseodymium doped ceria: Model mixed ionic electronic conductor with coupled electrical, optical, mechanical and chemical properties, *Solid State Ionics*, 2012, **225**, 194–197.
- D. Chen, Z. Guan, D. Zhang, L. Trotochaud, E. Crumlin, S. Nemsak, H. Bluhm, H. L. Tuller and W. C. Chueh, Constructing a pathway for mixed ion and electron transfer reactions for O_2 incorporation in $\text{Pr}_{0.1}\text{Ce}_{0.9}\text{O}_{2-x}$, *Nat. Catal.*, 2020, **3**, 116–124.
- N. Tsvetkov, Q. Lu, Y. Chen and B. Yildiz, Accelerated Oxygen Exchange Kinetics on $\text{Nd}_2\text{NiO}_{4+\delta}$ Thin Films with Tensile Strain along *c*-Axis, *ACS Nano*, 2015, **9**, 1613–1621.
- A. Egger, E. Bucher, W. Sitte, C. Lalanne and J. M. Bassat, Oxygen Exchange Kinetics and Chemical Stability of the IT-SOFC Cathode Material $\text{Nd}_2\text{NiO}_{4+\delta}$, *ECS Trans.*, 2019, **25**, 2547–2556.
- A. Murata, T. Uchikoshi and M. Matsuda, Fabrication and characterization of oriented $\text{Nd}_2\text{NiO}_{4+\delta}$ bulk and cathode for low-temperature operating solid oxide fuel cell, *J. Power Sources*, 2015, **293**, 95–100.
- H. Fukunaga, Reaction model of dense $\text{Sm}_{0.5}\text{Sr}_{0.5}\text{CoO}_{3-\delta}$ as SOFC cathode, *Solid State Ionics*, 2000, **132**, 279–285.



- 21 Z. Cai, M. Kubicek, J. Fleig and B. Yildiz, Chemical Heterogeneities on $\text{La}_{0.6}\text{Sr}_{0.4}\text{CoO}_{3-\delta}$ Thin Films – Correlations to Cathode Surface Activity and Stability, *Chem. Mater.*, 2012, **24**, 1116–1127.
- 22 M. Siebenhofer, C. Riedl, A. Schmid, A. Limbeck, A. K. Opitz, J. Fleig and M. Kubicek, Investigating oxygen reduction pathways on pristine SOFC cathode surfaces by *in situ* PLD impedance spectroscopy, *J. Mater. Chem. A*, 2022, **10**, 2305–2319.
- 23 C. Nicollet, C. Toparli, G. F. Harrington, T. Defferriere, B. Yildiz and H. L. Tuller, Acidity of surface-infiltrated binary oxides as a sensitive descriptor of oxygen exchange kinetics in mixed conducting oxides, *Nat. Catal.*, 2020, **3**, 913–920.
- 24 M. Riva, M. Kubicek, X. Hao, G. Franceschi, S. Gerhold, M. Schmid, H. Hutter, J. Fleig, C. Franchini, B. Yildiz and U. Diebold, Influence of surface atomic structure demonstrated on oxygen incorporation mechanism at a model perovskite oxide, *Nat. Commun.*, 2018, **9**, 3710.
- 25 G. M. Rupp, A. K. Opitz, A. Nanning, A. Limbeck and J. Fleig, Real-time impedance monitoring of oxygen reduction during surface modification of thin film cathodes, *Nat. Mater.*, 2017, **16**, 640–645.
- 26 D. Tripković, J. Wang, R. Küngas, M. B. Mogensen, B. Yildiz and P. V. Hendriksen, Thermally Controlled Activation and Passivation of Surface Chemistry and Oxygen-Exchange Kinetics on a Perovskite Oxide, *Chem. Mater.*, 2022, **34**, 1722–1736.
- 27 F. S. Baumann, J. Fleig, M. Konuma, U. Starke, H. U. Habermeier and J. Maier, Strong Performance Improvement of $\text{La}_{0.6}\text{Sr}_{0.4}\text{Co}_{0.8}\text{Fe}_{0.2}\text{O}_{3-\delta}$ SOFC Cathodes by Electrochemical Activation, *J. Electrochem. Soc.*, 2005, **152**, A2074.
- 28 G. M. Rupp, H. Tellez, J. Druce, A. Limbeck, T. Ishihara, J. Kilner and J. Fleig, Surface chemistry of $\text{La}_{0.6}\text{Sr}_{0.4}\text{CoO}_{3-\delta}$ thin films and its impact on the oxygen surface exchange resistance, *J. Mater. Chem. A*, 2015, **3**, 22759–22769.
- 29 G. M. Rupp, M. Kubicek, A. K. Opitz and J. Fleig, *In Situ* Impedance Analysis of Oxygen Exchange on Growing $\text{La}_{0.6}\text{Sr}_{0.4}\text{CoO}_{3-\delta}$ Thin Films, *ACS Appl. Energy Mater.*, 2018, **1**, 4522–4535.
- 30 D. Lee, R. Jacobs, Y. Jee, A. Seo, C. Sohn, A. V. Ievlev, O. S. Ovchinnikova, K. Huang, D. Morgan and H. N. Lee, Stretching Epitaxial $\text{La}_{0.6}\text{Sr}_{0.4}\text{CoO}_{3-\delta}$ for Fast Oxygen Reduction, *J. Phys. Chem. C*, 2017, **121**, 25651–25658.
- 31 R. Moreno, J. Zapata, J. Roqueta, N. Bagúes and J. Santiso, Chemical Strain and Oxidation-Reduction Kinetics of Epitaxial Thin Films of Mixed Ionic-Electronic Conducting Oxides Determined by X-Ray Diffraction, *J. Electrochem. Soc.*, 2014, **161**, F3046–F3051.
- 32 M. Kubicek, Z. Cai, W. Ma, B. Yildiz, H. Hutter and J. Fleig, Tensile Lattice Strain Accelerates Oxygen Surface Exchange and Diffusion in $\text{La}_{1-x}\text{Sr}_x\text{CoO}_{3-\delta}$ Thin Films, *ACS Nano*, 2013, **7**, 3276–3286.
- 33 Y. P. Ivanov, M. Kubicek, M. Siebenhofer, A. Viernstein, H. Hutter, J. Fleig, A. Chuvilin and Z. Zhang, Strain-induced structure and oxygen transport interactions in epitaxial $\text{La}_{0.6}\text{Sr}_{0.4}\text{CoO}_{3-\delta}$ thin films, *Commun. Mater.*, 2020, **1**, 25.
- 34 J. Wang, J. Yang, A. K. Opitz, D. Kalaev, A. Nanning, E. J. Crumlin, J. T. Sadowski, I. Waluyo, A. Hunt, H. L. Tuller and B. Yildiz, Strain-Dependent Surface Defect Equilibria of Mixed Ionic-Electronic Conducting Perovskites, *Chem. Mater.*, 2022, **34**, 5138–5150.
- 35 T. Mayeshiba and D. Morgan, Strain effects on oxygen migration in perovskites, *Phys. Chem. Chem. Phys.*, 2015, **17**, 2715–2721.
- 36 G. M. Rupp, M. Glowacki and J. Fleig, Electronic and ionic conductivity of $\text{La}_{0.95}\text{Sr}_{0.05}\text{Ga}_{0.95}\text{Mg}_{0.05}\text{O}_{3-\delta}$ single crystals, *J. Electrochem. Soc.*, 2016, **163**, F1189.
- 37 J. Januschewsky, M. Ahrens, A. Opitz, F. Kubel and J. Fleig, Optimized $\text{La}_{0.6}\text{Sr}_{0.4}\text{CoO}_{3-\delta}$ Thin-Film Electrodes with Extremely Fast Oxygen-Reduction Kinetics, *Adv. Funct. Mater.*, 2009, **19**, 3151–3156.
- 38 G. M. Rupp, A. Limbeck, M. Kubicek, A. Penn, M. Stöger-Pollach, G. Friedbacher and J. Fleig, Correlating surface cation composition and thin film microstructure with the electrochemical performance of lanthanum strontium cobaltite (LSC) electrodes, *J. Mater. Chem. A*, 2014, **2**, 7099–7108.
- 39 M. Siebenhofer, T. Huber, W. Artner, J. Fleig and M. Kubicek, Substrate stoichiometry changes during pulsed laser deposition: a case study on SrTiO_3 , *Acta Mater.*, 2021, **203**, 116461.
- 40 A. K. Opitz and J. Fleig, Investigation of O_2 reduction on Pt/YSZ by means of thin film microelectrodes: The geometry dependence of the electrode impedance, *Solid State Ionics*, 2010, **181**, 684–693.
- 41 T. Degen, M. Sadki, E. Bron, U. König and G. Néenert, The highscore suite, *Powder Diffr.*, 2014, **29**, S13–S18.
- 42 G. J. La O', S. J. Ahn, E. Crumlin, Y. Orikasa, M. D. Biegalski, H. M. Christen and Y. Shao-Horn, Catalytic Activity Enhancement for Oxygen Reduction on Epitaxial Perovskite Thin Films for Solid-Oxide Fuel Cells, *Angew. Chem., Int. Ed.*, 2010, **49**, 5344–5347.
- 43 B. Arndt, H. Noei, T. F. Keller, P. Müller, V. Vonk, A. Nanning, A. K. Opitz, J. Fleig, U. Rütt and A. Stierle, Structure and stability of Gd-doped CeO_2 thin films on yttrium-stabilized zirconia, *Thin Solid Films*, 2016, **603**, 56–61.
- 44 D. Nečas and P. Klapetek, Gwyddion: an open-source software for SPM data analysis, *Open Phys.*, 2012, **10**, 181–188.
- 45 L. A. Giannuzzi, J. L. Drown, S. R. Brown, R. B. Irwin and F. A. Stevie, Applications of the FIB lift-out technique for TEM specimen preparation, *Microsc. Res. Tech.*, 1998, **41**, 285–290.
- 46 A. Schmid, A. Nanning, A. Opitz, M. Kubicek and J. Fleig, High Oxygen Exchange Activity of Pristine $\text{La}_{0.6}\text{Sr}_{0.4}\text{FeO}_{3-\delta}$ Films and Its Degradation, *J. Electrochem. Soc.*, 2020, **167**, 124509.
- 47 A. Schmid, G. M. Rupp and J. Fleig, Voltage and partial pressure dependent defect chemistry in $(\text{La},\text{Sr})\text{FeO}_{3-\delta}$ thin films investigated by chemical capacitance measurements, *Phys. Chem. Chem. Phys.*, 2018, **20**, 12016–12026.
- 48 C. Riedl, M. Siebenhofer, A. Nanning, G. Friedbacher, M. Weiss, C. Rameshan, J. Bernardi, A. Limbeck, M. Kubicek,



- A. K. Opitz and J. Fleig, Performance modulation through selective, homogenous surface doping of lanthanum strontium ferrite electrodes revealed by *in situ* PLD impedance measurements, *J. Mater. Chem. A*, 2022, **10**, 2973–2986.
- 49 E. J. Crumlin, S. J. Ahn, D. Lee, E. Mutoro, M. D. Biegalski, H. M. Christen and Y. Shao-Horn, Oxygen Electrocatalysis on Epitaxial $\text{La}_{0.6}\text{Sr}_{0.4}\text{CoO}_{3-\delta}$ Perovskite Thin Films for Solid Oxide Fuel Cells, *J. Electrochem. Soc.*, 2012, **159**, F219–F225.
- 50 E. J. Crumlin, E. Mutoro, Z. Liu, M. E. Grass, M. D. Biegalski, Y. L. Lee, D. Morgan, H. M. Christen, H. Bluhm and Y. Shao-Horn, Surface strontium enrichment on highly active perovskites for oxygen electrocatalysis in solid oxide fuel cells, *Energy Environ. Sci.*, 2012, **5**, 6081.
- 51 C. Ahamer, A. K. Opitz, G. M. Rupp and J. Fleig, Revisiting the Temperature Dependent Ionic Conductivity of Yttria Stabilized Zirconia (YSZ), *J. Electrochem. Soc.*, 2017, **164**, F790–F803.
- 52 A. Schmid, G. M. Rupp and J. Fleig, Voltage and partial pressure dependent defect chemistry in $(\text{La},\text{Sr})\text{FeO}_{3-\delta}$ thin films investigated by chemical capacitance measurements, *Phys. Chem. Chem. Phys.*, 2018, **20**, 12016–12026.
- 53 S. Kogler, A. Nenning, G. M. Rupp, A. K. Opitz and J. Fleig, Comparison of Electrochemical Properties of $\text{La}_{0.6}\text{Sr}_{0.4}\text{FeO}_{3-\delta}$ Thin Film Electrodes: Oxidizing vs. Reducing Conditions, *J. Electrochem. Soc.*, 2015, **162**, F317–F326.
- 54 C. Riedl, M. Siebenhofer, A. Nenning, A. Schmid, M. Weiss, C. Rameshan, A. Limbeck, M. Kubicek, A. K. Opitz and J. Fleig, *In situ* techniques reveal the true capabilities of SOFC cathode materials and their sudden degradation due to omnipresent sulfur trace impurities, *J. Mater. Chem. A*, 2022, **10**, 14838–14848.
- 55 B. Koo, H. Kwon, Y. Kim, H. G. Seo, J. W. Han and W. Jung, Enhanced oxygen exchange of perovskite oxide surfaces through strain-driven chemical stabilization, *Energy Environ. Sci.*, 2018, **11**, 71–77.
- 56 A. Schmid and J. Fleig, The Current–Voltage Characteristics and Partial Pressure Dependence of Defect Controlled Electrochemical Reactions on Mixed Conducting Oxides, *J. Electrochem. Soc.*, 2019, **166**, F831–F846.
- 57 D. Marrocchelli, S. R. Bishop and J. Kilner, Chemical expansion and its dependence on the host cation radius, *J. Mater. Chem. A*, 2013, **1**, 7673.
- 58 V. Kharton, A. Yaremchenko, M. Patrakeev, E. Naumovich and F. Marques, Thermal and chemical induced expansion of $\text{La}_{0.3}\text{Sr}_{0.7}(\text{Fe},\text{Ga})\text{O}_{3-\delta}$ ceramics, *J. Eur. Ceram. Soc.*, 2003, **23**, 1417–1426.
- 59 D. Marrocchelli, N. H. Perry and S. R. Bishop, Understanding chemical expansion in perovskite-structured oxides, *Phys. Chem. Chem. Phys.*, 2015, **17**, 10028–10039.
- 60 Yu Chen and S. B. Adler, Thermal and Chemical Expansion of Sr-Doped Lanthanum Cobalt Oxide $\text{La}_{1-x}\text{Sr}_x\text{CoO}_{3-\delta}$, *Chem. Mater.*, 2005, **17**, 4537–4546.
- 61 S. Bishop, D. Marrocchelli, C. Chatzichristodoulou, N. Perry, M. Mogensen, H. Tuller and E. Wachsman, Chemical Expansion: Implications for Electrochemical Energy Storage and Conversion Devices, *Annu. Rev. Mater. Res.*, 2014, **44**, 205–239.
- 62 S. Wang, High temperature properties of $\text{La}_{0.6}\text{Sr}_{0.4}\text{Co}_{0.8}\text{Fe}_{0.2}\text{O}_{3-\delta}$ phase structure and electrical conductivity, *Solid State Ionics*, 2003, **159**, 71–78.
- 63 H. Lein, K. Wiik and T. Grande, Thermal and chemical expansion of mixed conducting $\text{La}_{0.5}\text{Sr}_{0.5}\text{Fe}_{1-x}\text{Co}_x\text{O}_{3-\delta}$ materials, *Solid State Ionics*, 2006, **177**, 1795–1798.
- 64 S. R. Bishop, K. L. Duncan and E. D. Wachsman, Thermo-Chemical Expansion in Strontium-Doped Lanthanum Cobalt Iron Oxide, *J. Am. Ceram. Soc.*, 2010, **93**, 4115–4121.
- 65 N. H. Perry, J. J. Kim, S. R. Bishop and H. L. Tuller, Strongly coupled thermal and chemical expansion in the perovskite oxide system $\text{Sr}(\text{Ti},\text{Fe})\text{O}_{3-\delta}$, *J. Mater. Chem. A*, 2015, **3**, 3602–3611.
- 66 X. Chen and T. Grande, Anisotropic Chemical Expansion of $\text{La}_{1-x}\text{Sr}_x\text{CoO}_{3-\delta}$, *Chem. Mater.*, 2013, **25**, 927–934.
- 67 X. Chen and T. Grande, Anisotropic and Nonlinear Thermal and Chemical Expansion of $\text{La}_{1-x}\text{Sr}_x\text{FeO}_{3-\delta}$ ($x = 0.3, 0.4, 0.5$) Perovskite Materials, *Chem. Mater.*, 2013, **25**, 3296–3306.
- 68 T. Grande, J. R. Tolchard and S. M. Selbach, Anisotropic Thermal and Chemical Expansion in Sr-Substituted LaMnO_3 : Implications for Chemical Strain Relaxation, *Chem. Mater.*, 2011, **24**, 338–345.
- 69 J. Fleig, G. M. Rupp, A. Nenning and A. Schmid, Towards an Improved Understanding of Electrochemical Oxygen Exchange Reactions on Mixed Conducting Oxides, *ECS Trans.*, 2017, **77**, 93–108.

